

Benchmarking Ionization Chambers, Microdiamond Detector, and Radiochromic Film for Small-Field Photon Dosimetry on an Elekta Versa HD

F. Er Radi^{1,3}, O. El mouden^{2*}, A. Bannan², Y. Himmi³, H. Rafik³, O. El Bounagui¹

¹LaMCSci, Faculty of Sciences, Mohammed V University in Rabat, Morocco

²Laboratory of Sciences and Engineering of Biomedicals, Biophysics and Health, Higher Institute of Health Sciences, Hassan 1st University, Settat, Morocco

³Casablanca International Oncology Center, Casablanca, Morocco

ABSTRACT Accurate small-field dosimetry remains detector-dependent, particularly for SRS-relevant apertures and highly modulated MLC patterns. This work benchmarks commonly available detectors on an Elekta Versa HD by comparing three ionization chambers (Farmer 0.6 cc, Semiflex 0.125 cc, PinPoint 3D 0.016 cc), a solid-state detector (PTW microDiamond 60019), and Gafchromic EBT3 film. Measurements were performed in water for 6 MV and 10 MV photon beams in flattened (FF) and flattening-filter-free (FFF) modes. Percent depth doses and lateral profiles were acquired for square fields across the small-field range, and relative output factors (OFs) were reported using a 5×5 cm² intermediate-field daisy-chain normalization. Static QA patterns (picket-fence 2-mm slits, step-and-shoot staircase, and an SRS 5×5-mm² small-segment grid) were evaluated at 10 cm depth using local 1D gamma analysis in a high-dose/high-gradient ROI, with comparisons performed against both the TPS and film. Detector dependence in OFs was maximal at 1×1 cm² and decreased rapidly with field size. Relative to film, microDiamond showed a consistent ≈+1.6% over-response at 1×1 cm² (e.g., 6 MV FF: 0.735 vs 0.723; 10 MV FF: 0.714 vs 0.702), while PinPoint 3D under-responded by -1.8% at 6 MV (e.g., 6 MV FFF: 0.714 vs 0.726) and by -3.8% at 10 MV (e.g., 10 MV FF: 0.676 vs 0.702; 10 MV FFF: 0.679 vs 0.705). At 2×2 cm², agreement improved (microDiamond +0.2–0.3%, PinPoint -0.3 to -0.4%, Semiflex ≈-0.7 to -0.8%), and by 3×3 cm² all systems converged toward film (typically ≤0.1%). For static QA patterns, mean (range) gamma pass rates versus TPS at 2%/2 mm were 97.0% (90.9–100) for microDiamond and 93.4% (77.3–100) for PinPoint, compared with 62.8% (22.7–80.2) for Semiflex and 44.7% (9.1–67.9) for Farmer; relaxing to 3%/3 mm increased pass rates to 98.9% and 98.4% (microDiamond/PinPoint), versus 80.7% and 58.3% (Semiflex/Farmer). Using film as reference reduced pass rates in the most modulated regions at 2%/2 mm (means: microDiamond 76.0%, PinPoint 76.9%, Semiflex 58.3%, Farmer 43.4%), and the TPS–film comparison itself reached 77.7% at 2%/2 mm. Overall, high-resolution systems (microDiamond and film) provided the most reliable performance for the smallest fields and highly modulated patterns, whereas ionization chambers especially larger volumes showed increasing volume-averaging effects that degrade OF accuracy and modulation fidelity; a 5×5 cm² daisy-chain normalization improved practical traceability when combining detectors across field sizes.

Keywords: Small-field dosimetry; Output factors; Output correction factor (OFC); Daisy-chain normalization; Elekta Versa HD; Flattening filter free (FFF); PTW microDiamond 60019; PinPoint 3D

Address for correspondence:

O. El mouden,
Laboratory of Sciences and Engineering of Biomedicals, Biophysics and Health,
Higher Institute of Health Sciences, Hassan 1st University, Settat, Morocco
E-mail: oussama.elmouden.doc@uhp.ac.ma

Word count: 7290 **Figure:** 11 **Tables:** 7 **References:** 39

Received: 01 Feb, 2026, Manuscript No. OAR-26-188449;

Editor assigned: 04 Feb, 2026, PreQC No. OAR-26-188449 (PQ);

Reviewed: 20 Feb, 2026, QC No. OAR-26-188449;

Revised: 25 Feb, 2026, Manuscript No. OAR-26-188449 (R);

Published: 28 Feb, 2026

INTRODUCTION

The widespread adoption of stereotactic radiosurgery (SRS), stereotactic body radiotherapy (SBRT), and highly modulated techniques (IMRT/VMAT) has increased the clinical reliance on small photon fields, where dose calculation and measurement uncertainties can translate into clinically relevant target underdosage or normal-tissue over-exposure [1–3]. In this regime, the field size becomes comparable to the projected source dimensions and to the lateral range of secondary electrons, leading to loss of lateral charged particle equilibrium, partial source occlusion, and strong sensitivity to collimation and detector geometry [1–3].

To mitigate these limitations, the IAEA/AAPM TRS-483 Code of Practice provides a unified framework for small-field reference and relative dosimetry, emphasizing the need for detector-specific output correction factors and consistent field definitions based on beam profiles (e.g., FWHM-based field size) [1,2]. This guidance builds upon the small-field formalism introduced by Alfonso et al., which explicitly separates the machine-specific field output factor from detector perturbations via correction factors that depend on field size and detector construction [2]. However, even with robust formalisms, the practical implementation remains challenging because no single detector is ideal across all small-field conditions, energies, and beam modalities (FF vs FFF) [1,2,4–6].

Among clinically available detectors, air-filled ionization chambers remain attractive for their stability and established calibration routes, yet their finite sensitive volumes can cause substantial volume-averaging and perturbation effects in steep dose gradients, affecting profiles, penumbrae, and output factors in very small fields [1,3,7]. Small-volume chambers (e.g., Semiflex 0.125 cc and PinPoint 3D 0.016 cc) reduce these effects but may still require careful consideration of polarity, recombination, stem effects, and orientation-dependent perturbations particularly in FFF beams with high dose-per-pulse [8–10]. Solid-state detectors such as the PTW microDiamond (60019) offer improved spatial resolution and near-tissue equivalence, but their response can still deviate in the smallest fields, motivating Monte Carlo and experimental studies to characterize and, when necessary, correct detector behavior [5,11,12].

In parallel, radiochromic film (Gafchromic EBT3) remains a high-value reference tool for small-field benchmarking due to its

sub-millimeter spatial resolution, near water equivalence at MV energies, and suitability for 2D dose mapping (profiles, penumbra, tongue-and-groove/MLC effects) [5,13–19]. Nevertheless, film dosimetry requires rigorous calibration and handling protocols (scanner response, orientation effects, inter-lot variability, post-irradiation growth, and multi-channel processing), which have been codified in AAPM guidance and refined by single-scan and adaptive calibration approaches [14,16,17,20].

Despite a growing literature on small-field detector correction factors and multicenter output-factor datasets [1,2,7,19,21–23], a practical need persists for clinically relevant benchmarking of commonly available ionization chambers (Farmer 0.6 cc, Semiflex 0.125 cc, PinPoint 3D 0.016 cc) against modern high-resolution detectors (microDiamond) and EBT3 film, specifically on the Elekta Versa HD platform and across FF/FFF beam qualities. The objective of this study is to quantify detector-dependent deviations in small-field dosimetry on a Versa HD by comparing a standard Farmer chamber (0.6 cc), two small-volume ionization chambers (Semiflex 0.125 cc and PinPoint 3D 0.016 cc), a microDiamond detector, and Gafchromic EBT3 film. Using clinically relevant square fields in the small-field range and both flattened and FFF beams (6 MV and 10 MV), we evaluate differences in (i) percent depth dose (PDD) curves, (ii) in-plane and cross-plane beam profiles at multiple depths, and (iii) output factors normalized to a 10×10 cm² reference field. In this approach, radiochromic film serves as a high-resolution reference for dose-gradient regions (penumbrae and off-axis tails), while the solid-state detector provides an alternative high-resolution point measurement. In addition, this work aims to enrich the current literature by providing a comprehensive Versa HD-specific benchmarking dataset, addressing the relative scarcity of multi-detector small-field dosimetry comparisons reported for this platform. The final goal is to provide practical recommendations for detector selection and measurement strategy for commissioning and patient-specific QA in small fields.

MATERIALS AND METHODS

Linear accelerator and beam qualities

Measurements were performed on an Elekta Versa HD linear accelerator (Elekta AB, Stockholm, Sweden) using clinical photon beams covering both flattened (FF) and flattening-filter-free (FFF) modalities. The beam set comprised 6 MV FF, 10 MV FF, 6 MV FFF, and 10 MV FFF photons, consistent with the commissioning dataset and detector-benchmarking datasheet used in this work. Beam quality was documented using standard clinical indices and depth-dose characteristics extracted from the commissioning data, including the depth of maximum dose (d_{max}) and a beam quality index (QI) based on the $TPR_{20/10}$ surrogate. In our dataset, the recorded values were: 6 MV FF (d_{max} = 16 mm, QI = 0.681), 10 MV FF (d_{max} = 22.5 mm, QI = 0.738). Dose calculations used for measurement comparison were generated in the RayStation treatment planning system (RayStation 2023B, RaySearch Laboratories, Stockholm, Sweden) using the site's commissioned Versa HD beam model; TPS-exported PDDs and lateral profiles were extracted for identical field definitions and normalization conventions to enable direct detector-to-TPS comparisons. These beam quality descriptors were used to ensure consistent comparisons across detectors and to interpret detector-dependent deviations as a function of beam energy and FF/FFF modality.

Detectors and dosimetry systems

The benchmarking dataset included three ionization chambers of different sensitive volumes, one solid-state detector, and radiochromic film used as a high-resolution reference [Table 1]. All point-detector measurements were acquired with a consistent detector axis and scan orientation for each beam/field configuration to minimize setup-dependent variability. EBT3 film was used to resolve high-gradient regions (penumbra and off-axis tails) where

Table 1: Detectors used in this study.

Device (model)	Type	Sensitive volume	Manufacturer (City, Country)	Main role in this study	Key strengths	Main limitations / notes (small fields)
Farmer 30013	Cylindrical ionization chamber	0.6 cm ³	PTW Freiburg GmbH (Freiburg, Germany)	Reference-like chamber for ≥5×5 cm ² trends; baseline comparison	Stable, robust, well-established calibration chain	Not recommended for very small fields: strong volume averaging in steep gradients; penumbra widening; OF systematic under-response and unstable readings in ≤4×4 cm ²
Semiflex 31010	Cylindrical ionization chamber	0.125 cm ³	PTW Freiburg GmbH (Freiburg, Germany)	Intermediate chamber for small fields down to ~3×3–5×5	Smaller volume than Farmer; good stability	Still affected by volume averaging in ≤2×2–3×3; orientation and positioning sensitivity in high gradients
PinPoint 3D 31022	Small-volume cylindrical ionization chamber	0.016 cm ³	PTW Freiburg GmbH (Freiburg, Germany)	Small-field chamber for ≤3×3 cm ² profiles/OFC	Better spatial resolution than larger chambers; ion chamber physics (no energy dependence issues typical of diodes)	Increased sensitivity to setup/positioning; potential signal-to-noise limitations; still not “film-like” resolution in penumbra
microDiamond 60019	Solid-state detector (diamond)	~0.004 mm ³	PTW Freiburg GmbH (Freiburg, Germany)	High-resolution point detector; comparator to film for small fields	High spatial resolution; near tissue equivalence; widely used for small-field commissioning	May require field/output correction factors in very small fields; angular dependence and detector-specific response must be considered
Gafchromic EBT3	Radiochromic film	N/A (2D dose map)	Ashland Inc. (Wilmington, DE, USA)	High-resolution reference for profiles/penumbra/complex gradients; cross-check OFC trends	Sub-mm spatial resolution; near water-equivalent response at MV; 2D mapping	Requires rigorous calibration + scanner protocol; sensitive to scanning artifacts, orientation, and post-irradiation development

finite-volume chambers are susceptible to volume-averaging effects.

Depth-dose curves and lateral beam profiles were acquired in a motorized 3D water phantom mounted on a SCANLIFT water-tank handling and reservoir system (PTW Freiburg GmbH, Freiburg, Germany). The SCANLIFT platform combines a mobile carriage/lift with an integrated water reservoir to facilitate filling/emptying and reproducible positioning of the water phantom in the treatment room. The scanning setup provided a measurement volume suitable for commissioning scans (typical scanning range for MP3-M configurations: $50 \times 50 \times 40.8 \text{ cm}^3$ in $X \times Y \times Z$), enabling high-resolution acquisition of PDDs and in-plane/cross-plane profiles across the investigated field sizes and depths [Figure 1].



Figure 1: Experimental setup for beam commissioning measurements on an Elekta Versa HD linear accelerator, showing the motorized 3D water phantom mounted on the SCANLIFT handling/reservoir system (PTW Freiburg GmbH, Freiburg, Germany) and positioned at the treatment isocenter for PDD and in-plane/cross-plane profile acquisitions.

Phantom, geometry, and field definitions

All measurements were performed in a motorized 3D water scanning phantom mounted on the SCANLIFT handling/reservoir system and aligned to the beam central axis. A consistent reference setup was used ($SSD = 100 \text{ cm}$), with depth scans acquired along the central axis (PDD) and lateral scans acquired along the in-plane and cross-plane directions. Square fields were defined using the multileaf collimator (MLC), with jaw settings specified to ensure a consistent collimation strategy across field sizes (e.g., jaw-tracking or fixed jaw margins). The $10 \times 10 \text{ cm}^2$ field was used as the reference for normalization of relative quantities. For small fields, an effective field size was additionally derived from the lateral profile FWHM, computed as the distance between the two 50% dose points (linear interpolation) after normalization to the central-axis value. The complete measurement geometry and field-definition settings are summarized in [Table 2].

Percent depth dose (PDD) measurements

Percent depth dose (PDD) curves were acquired in water for each photon beam quality (6 MV FF, 6 MV FFF, 10 MV FF, and 10 MV FFF) and for the investigated square field sizes using the motorized 3D scanning water phantom described above. Measurements were performed under a consistent reference geometry ($SSD = 100 \text{ cm}$) with the detector positioned on the beam central axis. For each detector type, the detector axis and orientation were kept constant for a given beam/field configuration, and the detector was carefully aligned to the beam central axis to minimize positioning uncertainty. PDD data were sampled from the near-surface region through deep depths to cover the clinically relevant range. To reduce ambiguity related to surface definition and detector-dependent effective measurement depth in the first millimeters, the analysis and reporting were restricted to depths $\geq 0.5 \text{ cm}$. For each beam quality and field size, PDDs were processed as relative

Table 2: Measurement geometry and field definitions used in this study.

Item	Definition / setting used	Rationale / notes
Linear accelerator	Elekta Versa HD (Elekta AB, Stockholm, Sweden)	Platform under investigation for small-field benchmarking
Phantom type	Motorized 3D water scanning phantom mounted on SCANLIFT (PTW Freiburg GmbH, Freiburg, Germany)	Water is the reference medium for relative dosimetry; SCANLIFT improves setup reproducibility
Setup position	Phantom aligned to beam central axis; setup performed under $SSD = 100 \text{ cm}$ reference geometry.	Ensures consistent geometry for PDD/profiles/output factors
Reference distance	$SSD = 100 \text{ cm}$ (unless stated otherwise)	Standard reference geometry for commissioning and relative dosimetry
Scan axes (lateral)	In-plane and cross-plane profiles	Captures anisotropy and MLC/gantry-related effects
Depth axis	Central-axis depth scan for PDD	Standard for beam quality and depth-dose characterization
Field shaping	Square, open MLC-defined fields	Clinically representative small-field delivery on Versa HD
Nominal field sizes	Small-field range emphasized ($\leq 3 \times 3 \text{ cm}^2$); $10 \times 10 \text{ cm}^2$ reference	Small fields are most sensitive to detector effects; 10×10 used for normalization
Field definition for analysis	Effective field size derived from profile FWHM (50%–50% points, linear interpolation after CAX normalization)	Required in small fields where penumbrae overlap and nominal settings may not represent delivered width
PDD normalization	PDD normalized to 100% at d_{max}	Enables shape-based comparison across detectors
Profile normalization	Profiles normalized to central-axis value (100%)	Allows robust comparison of width/penumbra/tails
Output normalization	OFC normalized to $10 \times 10 \text{ cm}^2$	Standard approach; enables inter-detector comparisons
Measurement depths (profiles)	d_{max} , 10 cm, 20 cm (typical)	Captures buildup + clinically relevant depths; consistent with commissioning practice
Detector positioning	Consistent detector axis/orientation for each configuration	Minimizes setup-dependent variability; critical in small fields
Data sampling	Typical step size: 0.5–1.0 mm in low-gradient regions and 0.1–0.2 mm in penumbra/high-gradient regions	Needed for reliable FWHM/80–20% penumbra extraction

depth–dose distributions and normalized to 100% at d_{max} to enable shape-based comparisons across detectors. Detector benchmarking was performed by using the microDiamond 60019 as the reference system for all PDD comparisons. Quantitative differences between detectors were evaluated at representative depths within build-up and beyond d_{max} (0.5, 1, 2, 10, and 20 cm). In addition, a 1D local gamma analysis of PDDs was performed against the microDiamond reference for selected fields and energies using criteria of 2%/2 mm and 3%/3 mm (local) over the depth range 0.5–25 cm, to characterize agreement trends in the build-up region versus the deeper depth–dose region.

Lateral beam profiles (in-plane and cross-plane)

Lateral beam profiles were measured in water for each photon beam quality (6 MV FF, 6 MV FFF, 10 MV FF, and 10 MV FFF) and for the investigated square field sizes using the motorized 3D scanning water phantom described above. Measurements were performed under a consistent reference geometry (SSD = 100 cm) with profiles acquired along the in-plane and cross-plane axes. While profile sets were collected at d_{max} , 10 cm, and 20 cm to sample build-up and clinically relevant depths, the primary detector-to-reference comparison and gamma-based evaluation reported in the Results section were performed at 10 cm depth for selected representative fields (e.g., 3×3, 5×5, 10×10, and 20×20 cm²).

For each detector type, the detector axis and scan orientation were kept constant for a given beam/field configuration, and careful alignment to the beam central axis was performed to minimize positioning uncertainty, which is particularly critical in small fields and steep-gradient regions. Measured profiles were processed as relative dose distributions and normalized to the central-axis value

(100%) to enable shape-based comparisons across detectors. From each profile, standard small-field metrics were extracted, including the full width at half maximum (FWHM) as an effective field-width descriptor, the 80–20% penumbra on both sides of the field, and the off-axis tail behavior outside the nominal field region [Figure 2]. For film measurements (Gafchromic EBT3), 2D dose maps were converted to dose and used to derive high-resolution in-plane and cross-plane line profiles through the field center, providing a benchmark for the penumbra and other high-gradient regions where finite-volume ionization chambers are prone to volume-averaging effects.

Output factors

Relative output factors (OFs), normalized to the 10×10 cm² reference field, were measured in water for all photon beam qualities (6 MV FF, 6 MV FFF, 10 MV FF, 10 MV FFF) using a consistent reference geometry (SSD = 100 cm) at a fixed reference depth. Detector readings were acquired on the beam central axis and corrected according to standard electrometer practice, including temperature–pressure correction for ionization chambers when applicable. Output factors were computed as: $OF(F) = \frac{M(F)}{M(10 \times 10)}$

Where $M(F)$ is the corrected detector signal for field size F . To ensure robust normalization in the very small-field regime, a daisy-chain (cross-normalization) approach was implemented by linking very small fields to the 10×10 cm² reference through an intermediate field F_{in} (typically 5×5 cm²), consistent with previously reported institutional methodology [5] and related commissioning workflows [4]. A detector suitable for reference/intermediate fields (e.g., a Farmer-type chamber, used only for $\geq 5 \times 5$ cm²) was used to establish $OF(F_{in})$ relative to 10×10 cm². A high-resolution small-

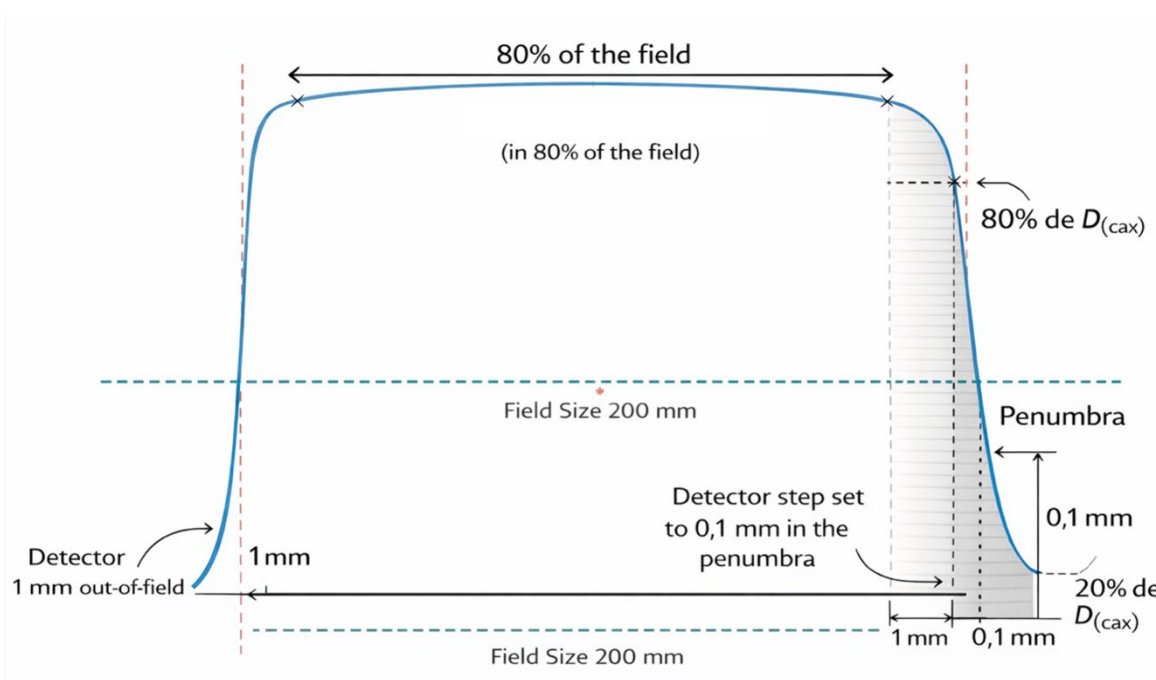


Figure 2: Schematic definition of lateral profile metrics and sampling strategy used in this study. The field width is evaluated from the central plateau, and the penumbra is defined as the lateral distance between the 80% and 20% dose levels relative to the central-axis dose D_{cax} . To accurately resolve high-gradient regions, the detector sampling step is set to 0.1 mm within the penumbra, while a coarser step (e.g., 1 mm) is used outside the field.

field detector (microDiamond and/or PinPoint 3D) was then used to measure the relative signal ratio between the small field F and F_{int} . The final OF for the smallest fields was obtained as:

$$OF(F) = OF(F_{int}) \times \frac{M_{SF}(F)}{M_{SF}(F_{int})}$$

Where M_{SF} denotes measurements acquired with the small-field detector. This strategy minimizes bias associated with using a single detector outside its recommended field-size range and supports consistent comparison of detector response against high-resolution references in fields $\leq 3 \times 3$ cm², where volume-averaging and detector-perturbation effects are most pronounced.

Gafchromic EBT3 film dosimetry and calibration workflow

Film irradiation and calibration

Gafchromic EBT3 radiochromic film (Ashland Inc., Wilmington, DE, USA) was used as a high-spatial-resolution dosimetry system for small-field benchmarking and as a reference in high-gradient regions. Calibration films were irradiated for each photon beam quality (6 MV FF, 6 MV FFF, 10 MV FF, and 10 MV FFF) using a consistent reference geometry (SSD = 100 cm) and a water-equivalent phantom. A series of known dose levels spanning the study range (0–600 cGy) was delivered to establish energy-specific dose–response curves. Specifically, 11 dose points were delivered at 0, 25, 50, 100, 150, 200, 300, 400, 450, 500, and 600 cGy, corresponding to a variable dose step of 25–100 cGy (denser sampling at low doses). Each calibration exposure was delivered as a single static irradiation with a fixed reference field (typically 10×10 cm²) at the calibration depth, using a consistent dose-per-MU calibration from the commissioning dataset. The delivered monitor units (MU) were calculated for each dose point using the machine output under reference conditions; in our calibration set this corresponded to approximately 25–600 MU across the 25–600 cGy dose range (1 MU per cGy under reference conditions, i.e., 100 MU per 1 Gy). After irradiation, all films (calibration and measurement) were stored under consistent ambient conditions and scanned after a fixed post-irradiation waiting time (24 h) to account for post-exposure development.

Film scanning and dose map processing

Films were digitized with a flatbed scanner in transmission mode using 48-bit RGB acquisition at 300 dpi (scanner settings kept constant for all scans), with all automatic image corrections disabled (e.g., color management, sharpening, dust removal, and auto-exposure). A scanner warm-up procedure was performed prior to acquisition, and all films were scanned with identical orientation and placed at a consistent position at the scanner center to minimize lateral-response effects. For each film, a central region of interest (ROI) of 20×20 mm² was analyzed at a fixed location relative to the irradiated field center. Net optical density (netOD) was computed using an unexposed film reference from the same lot: $netOD = \log_{10} \left(\frac{I_{unexp}}{I_{exp}} \right)$, where I_{unexp} and I_{exp} are the mean

pixel values measured in the ROI for unexposed and exposed films, respectively. No explicit scanner non-uniformity correction was applied; this effect was mitigated by consistent central placement of all films and by using an identical ROI extraction strategy for all scans. Dose conversion was performed using the red channel as the primary dosimetric channel, and a multichannel (RGB) approach was additionally implemented to improve robustness against scanner-related variability. Two-dimensional dose maps were then generated and used to extract high-resolution in-plane and cross-plane line profiles through the field center. Film-derived profiles were normalized to the central-axis dose (100%) and analyzed using the same metrics as the water-phantom scans, including FWHM, 80–20% penumbra, and off-axis tail behavior, enabling direct comparison with point-detector measurements and TPS calculations.

Data processing and comparison strategy

All datasets were exported in tabulated form and processed using a consistent coordinate system and normalization convention to enable direct inter-detector comparisons. For each beam quality and field size, PDD curves were normalized to 100% at d_{max} , and lateral profiles were normalized to the central-axis value (CAX = 100%). Relative output factors were reported as $OF(F) = M(F)/M(10 \times 10)$ under the same reference conditions, ensuring consistent normalization across detectors.

To account for differences in detector spatial resolution and sampling, lateral profile data were interpolated onto a common lateral grid when required before extracting profile-based metrics. Key metrics were extracted as follows: for PDDs, d_{max} relative dose values at clinically relevant depths (including shallow build-up points and 10 cm and 20 cm); for profiles, FWHM, 80–20% penumbra (left and right), and off-axis tail behavior; and for output factors, field-size-dependent trends with emphasis on the small-field range ($\leq 3 \times 3$ cm²).

Detector performance was evaluated against high-resolution references. EBT3 film was used as the primary benchmark for high-gradient regions (penumbra and dose tails) and for selected gamma-based profile comparisons, while microDiamond served as a high-resolution point-detector comparator for small-field profile and output-factor trends. Agreement was quantified using pointwise percentage differences and metric-based differences (e.g., $\Delta FWHM$, $\Delta penumbra$, ΔOF) as a function of field size, depth, and beam modality (FF vs FFF). For selected profiles and static QA patterns, agreement was additionally assessed using 1D local gamma analysis (2%/2 mm and 3%/3 mm) within a clinically relevant ROI defined on the reference distribution.

Static QA patterns and gamma analysis

Three static MLC QA patterns were delivered to probe detector performance under high-gradient, rapidly varying fluence conditions: (i) a picket-fence slit pattern, (ii) a step-and-shoot staircase modulation, and (iii) an SRS-type small-segment grid. All patterns were delivered for each photon beam quality (6 MV FF, 6 MV FFF, 10 MV FF, and 10 MV FFF) and measured in water at 10 cm depth under the same reference geometry (SSD = 100 cm)

used for profile benchmarking. Jaws were set to fully encompass the MLC-defined modulation region with a fixed margin (≥ 1 cm) to avoid jaw-induced truncation of the pattern.

Static pattern specifications

Picket-fence: a set of 11 narrow MLC slits was defined across the field, symmetric about the central axis. Each slit had an opening width of 2 mm, a length of 100 mm, and a uniform center-to-center spacing of 10 mm, generating a periodic peak–valley dose profile for spatial-resolution assessment.

Staircase (step-and-shoot): a sequence of 8 adjacent static segments was delivered to generate discrete dose plateaus with sharp transitions. Each segment had a fixed in-plane width of 20 mm (total modulated region 160 mm), while the segment relative weights were set to 100, 90, 80, 70, 60, 50, 40, and 30% of the maximum segment MU (normalized), producing a staircase-type intensity modulation.

SRS small-segment grid: an array of 5×5 square apertures (25 segments) was defined around the field center. Each aperture measured 5×5 mm², with a 10 mm pitch (center-to-center) in both directions, generating multiple sharp peaks separated by low-dose valleys representative of small-segment modulation.

Profile acquisition and normalization

For point detectors, 1D profiles were acquired along the in-plane axis through the pattern center and processed as relative dose distributions. For film (EBT3), 2D dose maps were reconstructed and a centered in-plane line profile was extracted using the same sampling convention. All static-pattern profiles were normalized to the central-axis value (100%) to allow direct comparison of modulation amplitude, peak broadening, and valley filling across detectors.

Gamma evaluation

Agreement was quantified using 1D local gamma analysis under criteria of 2%/2 mm and 3%/3 mm. Gamma was computed against two references: (a) the TPS-calculated profile and (b) the EBT3 film profile as a high-resolution experimental reference. Prior to gamma computation, profiles were interpolated to a common spatial grid (linear interpolation) when required. Gamma evaluation was restricted to a clinically relevant region of interest (ROI) defined as the set of points where the reference dose was $\geq 10\%$ of the profile maximum, limiting low-dose noise domination while retaining peak, penumbra, and modulation-edge regions. Gamma pass rate (%) was reported as the fraction of ROI points satisfying $\gamma \leq 1$, and results were summarized by

pattern, energy, and detector for comparison with the profile-overlay results.

RESULTS

Film calibration and dosimetric consistency (EBT3)

EBT3 film calibration demonstrated stable dose–response behavior across the investigated Versa HD photon beams (6 MV FF, 10 MV FF, 6 MV FFF, and 10 MV FFF). For each beam quality, net optical density (netOD) was measured over a wide dose range (0–600 cGy) and fitted using third-order polynomials to enable dose conversion for subsequent 2D film dosimetry. Calibration conditions (scanner, film lot, and post-irradiation waiting time) were kept constant to limit systematic variability [Table 3]. The resulting fits showed excellent agreement across energies and color channels, with $R^2 \geq 0.994$ and low fitting errors (RMSE/MAE in netOD units; [Table 4]). The red channel exhibited the highest sensitivity and the smoothest response over the investigated dose range [Figure 3], while the multichannel dataset (R/G/B) provided an illustrative example of channel-dependent sensitivity and uncertainty behavior [Figure 4–6] (MV FF). Residuals of the red-channel fits remained small and centered around zero for all beam qualities [Figure 5], supporting the use of these calibration curves for subsequent profile extraction, detector benchmarking, and film-referenced comparisons.

Percent depth dose (PDD)

Percent depth dose (PDD). PDD curves were compared across detectors using the microDiamond 60019 as the reference. Overall, agreement among the three ionization chambers was energy dependent and was strongest beyond the build-up region. For the 10×10 cm² reference field, deviations relative to microDiamond remained small at clinical depths, while the largest detector-dependent differences occurred in the build-up region, particularly for the Farmer chamber [Table 5]. For 6 MV FF, differences versus microDiamond at 0.5 cm ranged from –6.61% (Farmer) to –0.12% (PinPoint 3D), and at 1 cm from –2.61% (Farmer) to –0.18% (PinPoint 3D) (Table 5). At 10 cm and 20 cm, agreement improved, with differences versus microDiamond confined to +0.04% to +0.65% (10 cm) and +0.07% to +0.60% (20 cm) across ionization chambers [Table 5]. For 10 MV FF, the Farmer again showed the largest build-up discrepancy (up to –7.42% at 0.5 cm and –2.82% at 1 cm relative to microDiamond), whereas Semiflex and PinPoint 3D remained closer to microDiamond [Table 5]. For 6 MV FFF, Farmer deviations relative to microDiamond reached –6.42% (0.5 cm) and –2.54% (1 cm), whereas Semiflex and PinPoint 3D stayed within –0.2–0.6% in

Table 3: EBT3 calibration dataset and acquisition conditions.

Energy	Calibration points (n)	Dose range (cGy)	Scanner	Film lot	Wait time (h)	netOD uncertainty (mean ± max, 1σ)
6 MV FF	11	0–600	EPSON 10000XL	EBT3_Lot_A	24	0.0102 ± 0.0140
10 MV FF	11	0–600	EPSON 10000XL	EBT3_Lot_A	24	0.0102 ± 0.0140
6 MV FFF	11	0–600	EPSON 10000XL	EBT3_Lot_A	24	0.0102 ± 0.0140
10 MV FFF	11	0–600	EPSON 10000XL	EBT3_Lot_A	24	0.0102 ± 0.0140

Table 4: Polynomial fit performance by energy and channel ($\text{netOD} = a_3 \cdot D^3 + a_2 \cdot D^2 + a_1 \cdot D + a_0$).

Energy	Channel	R ²	RMSE (netOD)	MAE (netOD)
6 MV FF	R	0.999652	0.003261	0.002847
6 MV FF	G	0.999177	0.003746	0.00316
6 MV FF	B	0.998586	0.003162	0.002602
10 MV FF	R	0.999647	0.003385	0.002806
10 MV FF	G	0.999381	0.003138	0.002731
10 MV FF	B	0.994546	0.006205	0.00518
6 MV FFF	R	0.999509	0.003909	0.00308
6 MV FFF	G	0.998902	0.004208	0.003466
6 MV FFF	B	0.999338	0.002186	0.001719
10 MV FFF	R	0.999439	0.004265	0.003765
10 MV FFF	G	0.999393	0.003115	0.002333
10 MV FFF	B	0.998892	0.002925	0.002378

Figure 3 — EBT3 dose-response (Red channel): FF vs FFF beams

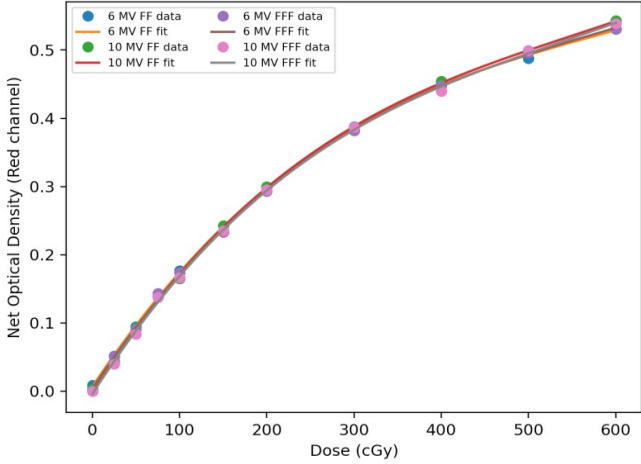


Figure 3: EBT3 film calibration curves (red channel) for Elekta Versa HD photon beams: 6 MV FF, 10 MV FF, 6 MV FFF, and 10 MV FFF. Measured net optical density (netOD) values are shown with the corresponding fitted polynomial dose-response curves over the calibration range (0–600 cGy).

Figure 4 — EBT3 multichannel calibration (6 MV FF) with 1σ netOD uncertainty

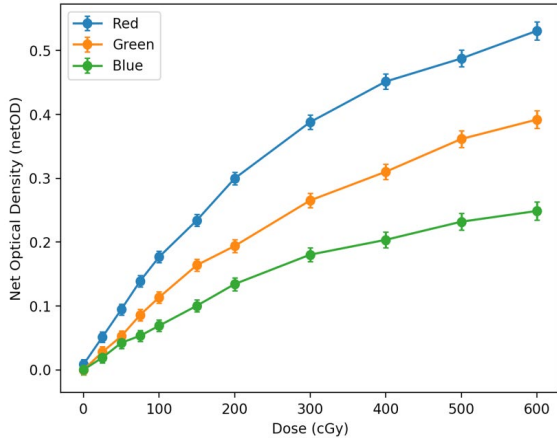


Figure 4: Representative multichannel (RGB) EBT3 calibration for the 6 MV FF beam. Net optical density (netOD) measurements are shown for the red, green, and blue channels with 1σ uncertainty bars (computed from repeated ROI sampling under identical scanning conditions), illustrating channel-dependent sensitivity and measurement variability across the 0–600 cGy calibration range.

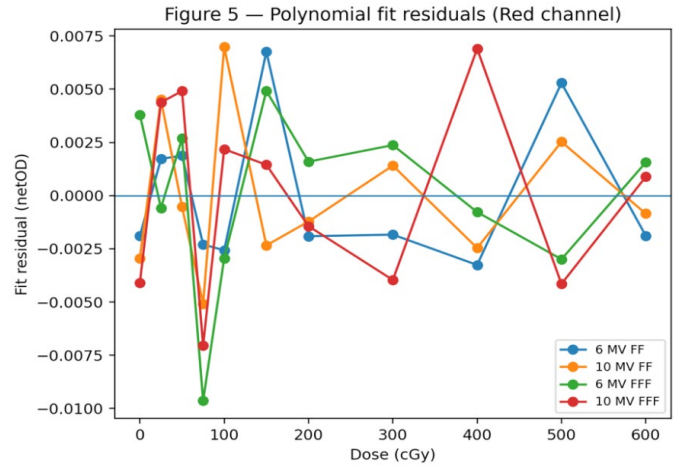


Figure 5: Residual analysis of the EBT3 red-channel calibration fits for all beam qualities (6 MV FF, 10 MV FF, 6 MV FFF, and 10 MV FFF). Residuals (fit – measurement) are plotted as a function of dose, demonstrating the goodness-of-fit and the absence of systematic bias over the full calibration range.

the build-up and within $\leq 1\%$ at 10–20 cm [Table 5]. For 10 MV FFF, Farmer differences peaked at -7.56% (0.5 cm) and -2.95% (1 cm); the small-volume chambers remained within $\sim 0.3\text{--}0.6\%$ at 0.5–1 cm and within $\sim 0.1\text{--}0.8\%$ at 10–20 cm [Table 5]. Across all energies, the apparent d_{max} shift relative to microDiamond was smallest for PinPoint 3D (typically 0–1 mm) and larger for the Farmer chamber (up to ~ 2 mm), consistent with the effect of finite sensitive volume and reduced depth sampling resolution in the build-up region [Table 5]. These observations are supported by the local gamma analysis in [Figure 6], where elevated γ values are concentrated in the build-up region and rapidly decrease to $\gamma < 1$ beyond d_{max} for the small-volume chambers across energies and field sizes. Full PDD results for all field sizes ($5 \times 5\text{--}40 \times 40$ cm²) and energies are reported in [Appendix Table A1].

Lateral beam profiles (in-plane and cross-plane)

Lateral beam profiles were evaluated at 10 cm depth in both in-plane and cross-plane directions using local 1D gamma analysis within a clinically relevant ROI spanning the central region and penumbra ($\pm[\text{half-field} + 20$ mm]). To keep the main manuscript focused, [Figure 7], presents representative dose-profile overlays (3×3 and 5×5 cm² across energies), whereas [Figure 8] reports representative gamma-index distributions for 3×3 and 5×5 cm². Under the more stringent 2%/2 mm criterion, the smallest fields (3×3 and 5×5 cm²) consistently produced the largest gamma excursions, with failures concentrated around the high-gradient penumbra, reflecting the combined impact of detector spatial resolution, volume averaging, and positioning sensitivity [Figure 8]. In contrast, 10×10 cm² profiles showed markedly improved agreement and more uniformly low gamma values across the field, and 20×20 cm² exhibited the highest overall consistency, with gamma deviations largely confined to the extreme off-axis tails. Across all beams (FF and FFF, 6 and 10 MV), the detector-dependent pattern remained stable: microDiamond and EBT3 film provided the most robust agreement in edge regions, whereas the Farmer chamber showed the most pronounced penumbra broadening and corresponding gamma degradation, especially in

Table 5: Percent depth dose (PDD) metrics for the 10×10 cm² reference field (normalized to TPS dmax).

Beam	Detector	dmax (cm)	Δdmax vs microDiamond (mm)	ΔPDD 0.5 cm (%)	ΔPDD 1 cm (%)	ΔPDD 2 cm (%)	ΔPDD 10 cm (%)	ΔPDD 20 cm (%)
6 MV FF	PinPoint 3D 0.016 cc	1.6	0	-0.12	-0.18	0	0.01	0.07
6 MV FF	Semiflex 0.125 cc	1.65	0.5	-0.30	-0.34	-0.16	0.26	0.2
6 MV FF	Farmer 0.6 cc	1.8	2	-6.61	-2.61	0.27	0.65	0.6
10 MV FF	PinPoint 3D 0.016 cc	2.3	1	-0.34	-0.22	-0.03	0.12	0.03
10 MV FF	Semiflex 0.125 cc	2.25	0.5	-0.62	-0.39	-0.10	0.16	0.11
10 MV FF	Farmer 0.6 cc	2.1	-1.0	-7.42	-2.82	-0.57	0.87	0.58
6 MV FFF	PinPoint 3D 0.016 cc	1.7	0	-0.24	-0.05	0	0.05	0.2
6 MV FFF	Semiflex 0.125 cc	1.65	-0.5	-0.59	-0.27	-0.11	0.1	0.14
6 MV FFF	Farmer 0.6 cc	1.7	0	-6.79	-2.74	0.08	0.95	0.58
10 MV FFF	PinPoint 3D 0.016 cc	2.5	-0.5	-0.25	-0.15	0	0.04	0.06
10 MV FFF	Semiflex 0.125 cc	2.6	0.5	-0.47	-0.33	-0.13	-0.04	0.25
10 MV FFF	Farmer 0.6 cc	2.65	1	-7.56	-2.95	-0.56	0.62	0.73

Figure 6 — Local 1D gamma analysis of PDDs vs microDiamond reference
 Criterion: 2%/2 mm (local), depth range: 0.5–25 cm; fields: 3×3, 5×5, 10×10, 20×20 cm²

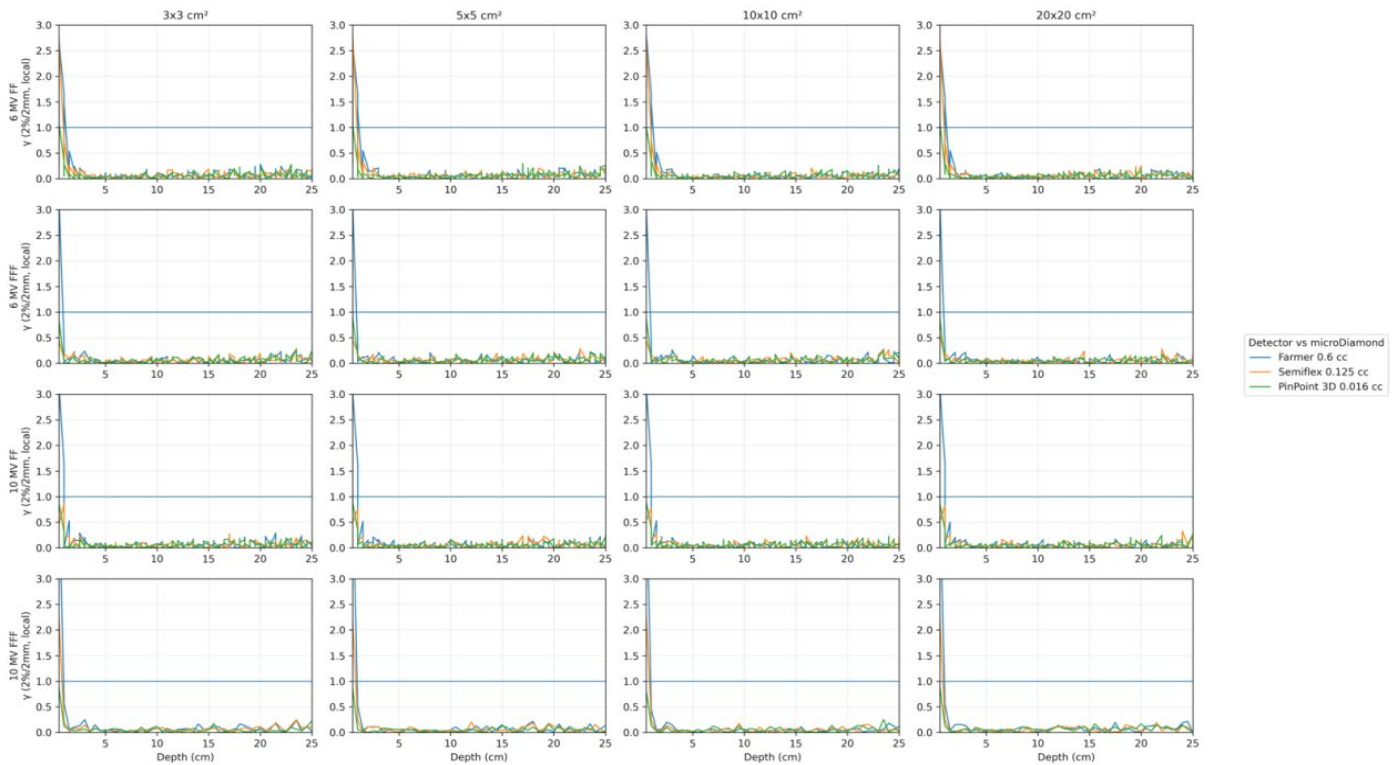


Figure 6: Local 1D gamma analysis of measured PDD curves referenced to the microDiamond detector. Gamma profiles were calculated in water over 0.5–25 cm depth using (top) 2%/2 mm (local) and (bottom) 3%/3 mm (local) criteria for the square fields 3×3, 5×5, 10×10, and 20×20 cm². Rows correspond to photon beam qualities (6 MV FF, 6 MV FFF, 10 MV FF, 10 MV FFF) and columns to field size. Curves represent each ionization chamber compared against the microDiamond reference: Farmer 0.6 cc (30013), Semiflex 0.125 cc (31010), and PinPoint 3D 0.016 cc (31022). The horizontal line at $\gamma = 1$ indicates the pass/fail threshold. Across energies and field sizes, gamma values are highest in the build-up region and decrease rapidly beyond dmax, with the largest deviations typically observed for the Farmer chamber due to finite-volume effects.

the smallest fields [Figures 7, 8]. When switching the reference from TPS to EBT3 film, gamma performance in 3×3 and 5×5 cm² tended to decrease modestly, consistent with film’s higher sensitivity to subtle edge-shape discrepancies that may be partially smoothed in TPS dose modeling; this effect was much less evident for 10×10 and 20×20 cm² [Figure 8].

Output factors (small-field relative output) and daisy-chain implementation

Relative output factors (OFs) were renormalized to the 5×5 cm² intermediate field (daisy-chain link) to reduce normalization bias when combining detectors with different optimal field-size ranges.

Lateral beam profiles at depth 10 cm — 3×3 and 5×5 cm² (all energies)
(corrected logical detector-dependent broadening)

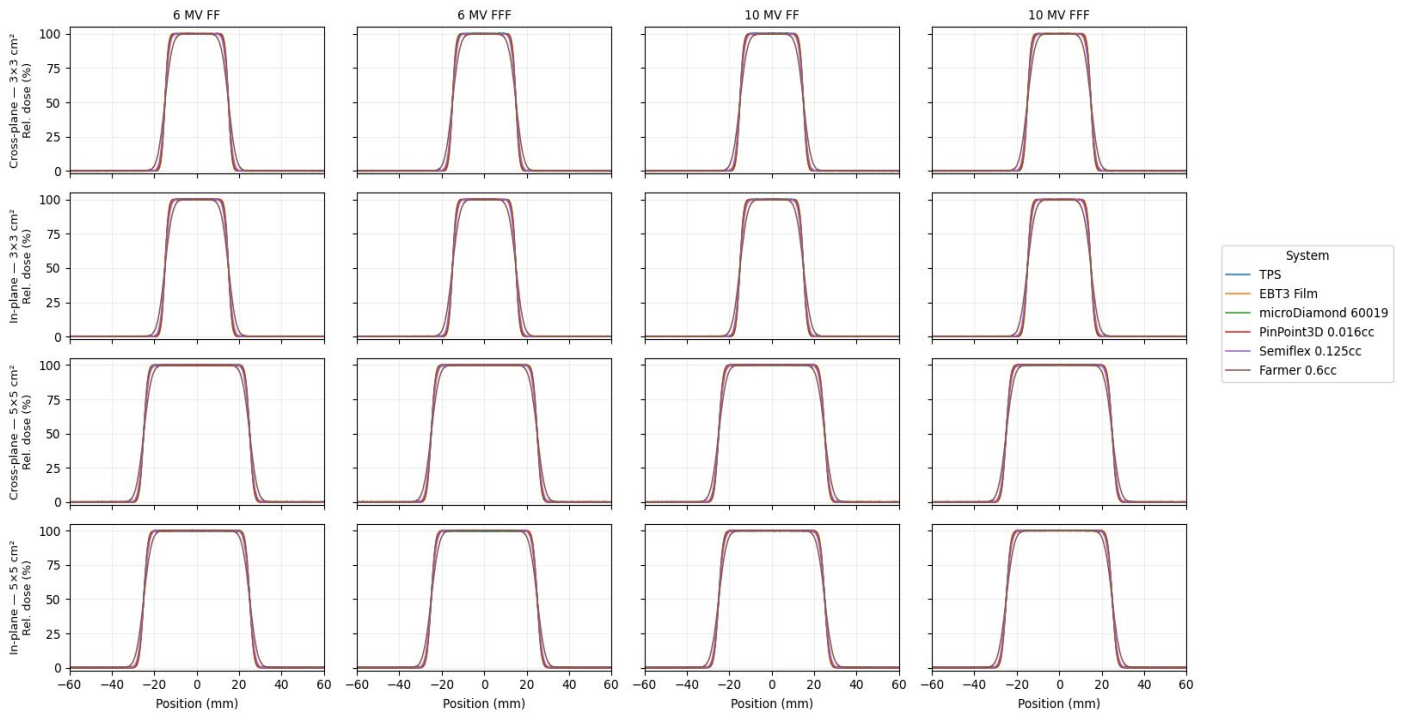


Figure 7: Lateral beam profile overlays measured at 10 cm depth for small square fields (3×3 and 5×5 cm²) on the Elekta Versa HD. Cross-plane profiles are shown in the top two rows and in-plane profiles in the bottom two rows. Columns correspond to the four photon beam qualities: 6 MV FF, 6 MV FFF, 10 MV FF, and 10 MV FFF. All profiles are presented as relative dose normalized to the central axis (CAX = 100%) and plotted for the TPS calculation and the five measurement systems (EBT3 film, microDiamond 60019, PinPoint 3D 0.016 cc, Semiflex 0.125 cc, Farmer 0.6 cc). The figure highlights detector-dependent differences in penumbra width and edge steepness, with the largest-volume chamber (Farmer) exhibiting the most pronounced profile broadening in the smallest fields.

Gamma index (clean legend) — In-plane — 6 MV FF — depth 10 cm
(3×3 and 5×5 cm²)

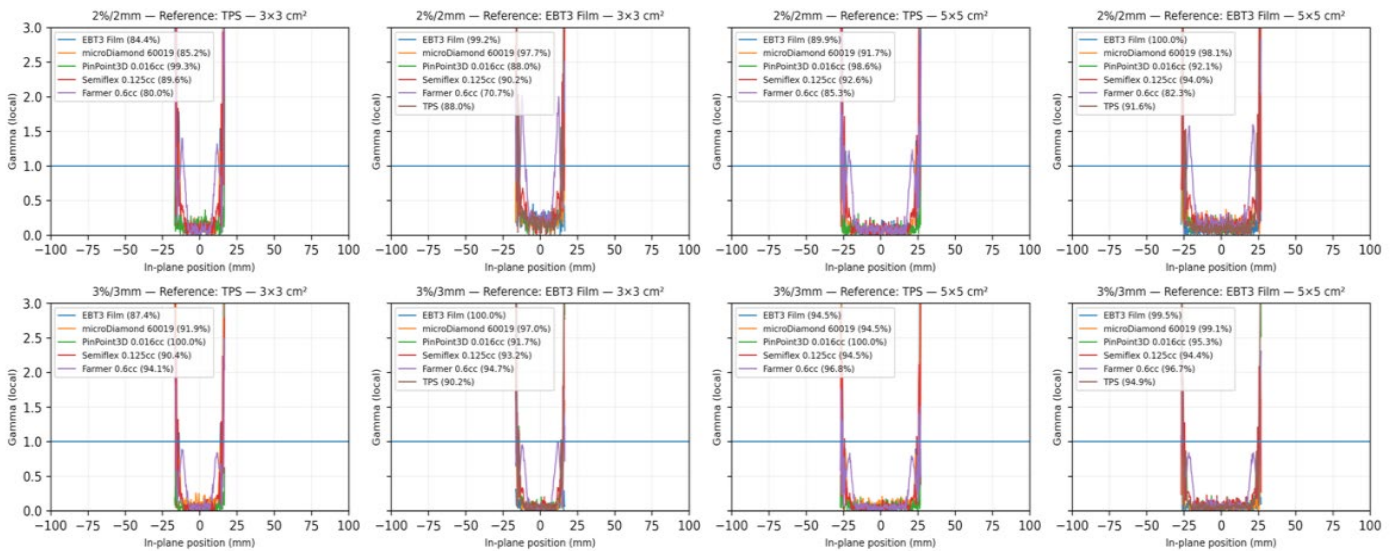


Figure 8: Local 1D gamma-index distributions for in-plane lateral profiles measured at 10 cm depth for 3×3 cm² and 5×5 cm² fields in the 6 MV FF beam. Gamma was computed using 2%/2 mm (top row) and 3%/3 mm (bottom row) criteria, and evaluated using two different references: TPS (left panels) and Gafchromic EBT3 film (right panels). Curves correspond to the comparison of each detector/system (microDiamond 60019, PinPoint 3D 0.016 cc, Semiflex 0.125 cc, Farmer 0.6 cc, and film) against the selected reference. The horizontal line at $\gamma = 1$ indicates the pass/fail threshold, and the percentage values in the legend report the gamma pass rate within the ROI for each detector. Elevated gamma values are primarily localized in the high-gradient penumbra region, while the central plateau shows consistently low γ values, with more pronounced excursions for larger-volume chambers in the smallest field.

Table 6: Consolidated small-field output summary (reference = EBT3 film).

Field (cm ²)	Film OF _{5x5}	microDiamond OF _{5x5} (Δ vs film)	PinPoint OF _{5x5} (Δ vs film)	Semiflex OF _{5x5} (Δ vs film)
1x1	0.723	0.735 (+1.6%)	0.711 (-1.8%)	—
2x2	0.851	0.853 (+0.2%)	0.849 (-0.3%)	0.845 (-0.8%)
3x3	0.936	0.936 (+0.0%)	0.936 (+0.0%)	0.935 (-0.1%)
5x5	1	1.000 (+0.0%)	1.000 (+0.0%)	1.000 (+0.0%)
10x10	1.064	1.064 (+0.0%)	1.064 (+0.0%)	1.064 (+0.0%)

6 MV FFF

Field (cm ²)	Film OF _{5x5}	microDiamond OF _{5x5} (Δ vs film)	PinPoint OF _{5x5} (Δ vs film)	Semiflex OF _{5x5} (Δ vs film)
1x1	0.726	0.738 (+1.6%)	0.714 (-1.8%)	—
2x2	0.853	0.855 (+0.2%)	0.851 (-0.3%)	0.847 (-0.7%)
3x3	0.937	0.937 (+0.0%)	0.937 (+0.0%)	0.936 (-0.1%)
5x5	1	1.000 (+0.0%)	1.000 (+0.0%)	1.000 (+0.0%)
10x10	1.053	1.053 (+0.0%)	1.053 (+0.0%)	1.053 (+0.0%)

6 MV FF

Field (cm ²)	Film OF _{5x5}	microDiamond OF _{5x5} (Δ vs film)	PinPoint OF _{5x5} (Δ vs film)	Semiflex OF _{5x5} (Δ vs film)
1x1	0.702	0.714 (+1.6%)	0.676 (-3.8%)	—
2x2	0.84	0.843 (+0.3%)	0.837 (-0.4%)	0.833 (-0.8%)
3x3	0.926	0.926 (+0.0%)	0.925 (-0.1%)	0.925 (-0.1%)
5x5	1	1.000 (+0.0%)	1.000 (+0.0%)	1.000 (+0.0%)
10x10	1.064	1.064 (+0.0%)	1.064 (+0.0%)	1.064 (+0.0%)

10 MV FF

Field (cm ²)	Film OF _{5x5}	microDiamond OF _{5x5} (Δ vs film)	PinPoint OF _{5x5} (Δ vs film)	Semiflex OF _{5x5} (Δ vs film)
1x1	0.705	0.717 (+1.6%)	0.679 (-3.7%)	—
2x2	0.842	0.844 (+0.2%)	0.839 (-0.4%)	0.836 (-0.7%)
3x3	0.926	0.926 (+0.0%)	0.925 (-0.1%)	0.925 (-0.1%)
5x5	1	1.000 (+0.0%)	1.000 (+0.0%)	1.000 (+0.0%)
10x10	1.053	1.053 (+0.0%)	1.053 (+0.0%)	1.053 (+0.0%)

10 MV FFF

Note: Farmer 0.6 cc (small fields): for ≤3x3 cm², Farmer is expected to show a systematic under-response (order of a few % up to >5% depending on field definition and setup) due to severe volume averaging; it should not be used for reporting small-field OFs and is best restricted to reference / intermediate fields within the daisy-chain.

With this convention, OFs increased monotonically with field size for all beam qualities (6 MV FF, 6 MV FFF, 10 MV FF, 10 MV FFF), and the detector-dependent spread was most pronounced in the very small-field domain (≤3x3 cm²) [Table 6], [Figure 9].

Using Gafchromic EBT3 film as the reference, microDiamond 60019 showed a small systematic over-response in the smallest field, consistent with TRS-483 trends: at 1x1 cm², the microDiamond-to-film difference was +1.6% for all beams (e.g., 6 MV FF: OF_{5x5} = 0.735 vs 0.723 for film; 10 MV FF: 0.714 vs 0.702) [Table 6]. Conversely, the PinPoint 3D (0.016 cc) exhibited an under-response at 1x1 cm², with deviations of -1.8% for 6 MV and -3.8% for 10 MV (e.g., 10 MV FF: OF_{5x5} = 0.676 vs 0.702 for film; 10 MV FFF: 0.679 vs 0.705) [Table 6]. For 2x2 cm², inter-detector agreement improved substantially: microDiamond remained within +0.2–0.3%, PinPoint within -0.2 to -0.4%, and Semiflex showed the largest residual under-response (≈-0.7 to -0.8%) [Table 6]. At 3x3 cm², all systems converged closely to the film reference (typically ≤0.1% difference for PinPoint and Semiflex, and ~0% for microDiamond), and agreement was essentially indistinguishable at ≥5x5 cm² [Table 6]. The expected energy dependence was preserved, with larger departures from

unity for the chamber-based systems at 10 MV than at 6 MV, particularly at 1x1 cm² for PinPoint [Figure 9].

Static QA patterns and gamma analysis

For the static QA field patterns (picket-fence, step-and-shoot staircase, and SRS small-segment grid) evaluated at 10 cm depth, agreement was quantified using 1D local gamma analysis within a clinically relevant ROI focusing on the high-dose and high-gradient region [Figure 10, 11]. Overall, microDiamond and PinPoint 3D showed the most consistent agreement with the TPS across beam qualities, whereas Semiflex demonstrated intermediate performance and the Farmer chamber yielded the poorest agreement, consistent with strong volume-averaging in rapidly varying dose patterns [Figure 11]. When film was used as the reference, gamma pass rates generally decreased compared with TPS-reference particularly in steep gradients reflecting the higher spatial fidelity of film at modulation edges and low-dose tails [Figure 10].

Across all static QA patterns and energies, the mean (range) gamma pass rate vs TPS for 2%/2 mm was 97.0% (90.9–100%)

Figure 9 — Small-field output correction behavior vs EBT3 film (TRS-483-consistent trends)
 $k = \text{Film OF} / \text{Detector OF}$; bias = $(1/k - 1) \times 100\%$

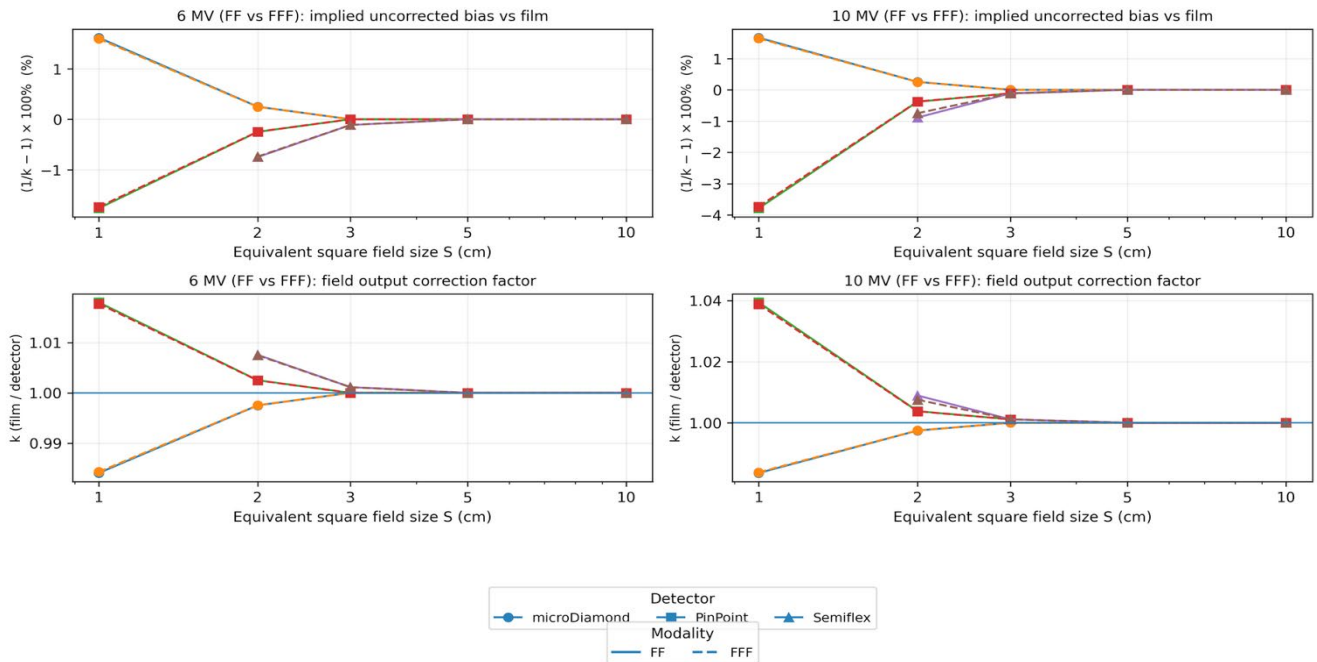


Figure 9: Small-field output correction behavior relative to Gafchromic EBT3 film (TRS-483-consistent trends). Field output correction factors k were derived using EBT3 film as the reference, with $k = \text{Film OF} / \text{Detector OF}$, and the corresponding implied uncorrected detector bias expressed as $(1/k - 1) \times 100\%$. Results are shown as a function of equivalent square field size S (cm) for 6 MV (left column) and 10 MV (right column), including flattened (FF) and flattening-filter-free (FFF) beams (line style). The top row reports the implied uncorrected bias vs film, while the bottom row shows the correction factors k (horizontal line at $k=1$ indicates perfect agreement with film). Curves are displayed for microDiamond 60019, PinPoint 3D (0.016 cc), and Semiflex (0.125 cc) (marker style), demonstrating increasing deviation from unity as field size decreases, with larger departures typically observed at $1 \times 1 \text{ cm}^2$ and for 10 MV beams.

Table 7: Static QA field agreement metrics at 10 cm depth (all energies pooled).

Detector / system	Gamma pass rate vs TPS (%) 2%/2 mm	Gamma pass rate vs TPS (%) 3%/3 mm	Gamma pass rate vs Film (%) 2%/2 mm	Gamma pass rate vs Film (%) 3%/3 mm	MAE vs TPS in ROI (%)
microDiamond 60019	97.0 (90.9–100)	98.9 (90.9–100)	76.0 (45.5–93.8)	85.4 (54.5–95.1)	0.35
PinPoint 3D 0.016 cc	93.4 (77.3–100)	98.4 (95.5–100)	76.9 (40.9–92.6)	86.6 (50.0–96.3)	0.45
Semiflex 0.125 cc	62.8 (22.7–80.2)	80.7 (54.5–92.6)	58.3 (13.6–77.8)	77.9 (40.9–91.4)	1.32
Farmer 0.6 cc	44.7 (9.1–67.9)	58.3 (13.6–76.5)	43.4 (0.0–69.1)	58.3 (18.2–76.5)	3.23
TPS vs EBT3 Film	77.7 (40.9–95.1)	87.9 (59.1–98.3)	—	—	0.8

(Values are mean (min–max) pooled over the three static patterns and all energies. MAE = mean absolute error vs TPS within the ROI.)

for microDiamond and 93.4% (77.3–100%) for PinPoint 3D, compared with 62.8% (22.7–80.2%) for Semiflex and 44.7% (9.1–67.9%) for the Farmer chamber. Relaxing criteria to 3%/3 mm increased pass rates for all detectors, reaching 98.9% (90.9–100%) for microDiamond and 98.4% (95.5–100%) for PinPoint 3D, while Semiflex improved to 80.7% (54.5–92.6%) and Farmer to 58.3% (13.6–76.5%). Using film as the reference, mean pass rates were lower in the most modulated regions: for 2%/2 mm, microDiamond and PinPoint averaged 76.0% and 76.9%, while Semiflex and Farmer averaged 58.3% and 43.4%; under 3%/3 mm, these increased to 85.4% (microDiamond), 86.6% (PinPoint), 77.9% (Semiflex), and 58.3% (Farmer). The TPS–film comparison itself achieved 77.7% at 2%/2 mm and 87.9% at 3%/3 mm, indicating that part of the apparent detector-to-TPS disagreement originates from TPS smoothing/modeling relative to film’s high-resolution response in high-gradient structures.

DISCUSSION

This study quantified, on an Elekta Versa HD, the impact of detector selection on three major components of small-field dosimetry: percent depth dose (PDD), lateral beam profiles, and relative output factors / output correction factors (OF/FOC), with an extension to static QA patterns and local 1D gamma analysis. The overall trends observed are consistent with international reference frameworks and the experimental/Monte Carlo literature: as field size decreases, measurements become increasingly dominated by (i) finite detector size and volume averaging, (ii) detector-induced perturbation effects, (iii) positioning sensitivity, and (iv) lateral charged-particle disequilibrium and spectral hardening, as explicitly discussed in IAEA TRS-483 and the formalism of Alfonso et al. through the small-field correction factor $k_{Q,lin,Q_{ref}}$ [1,2].

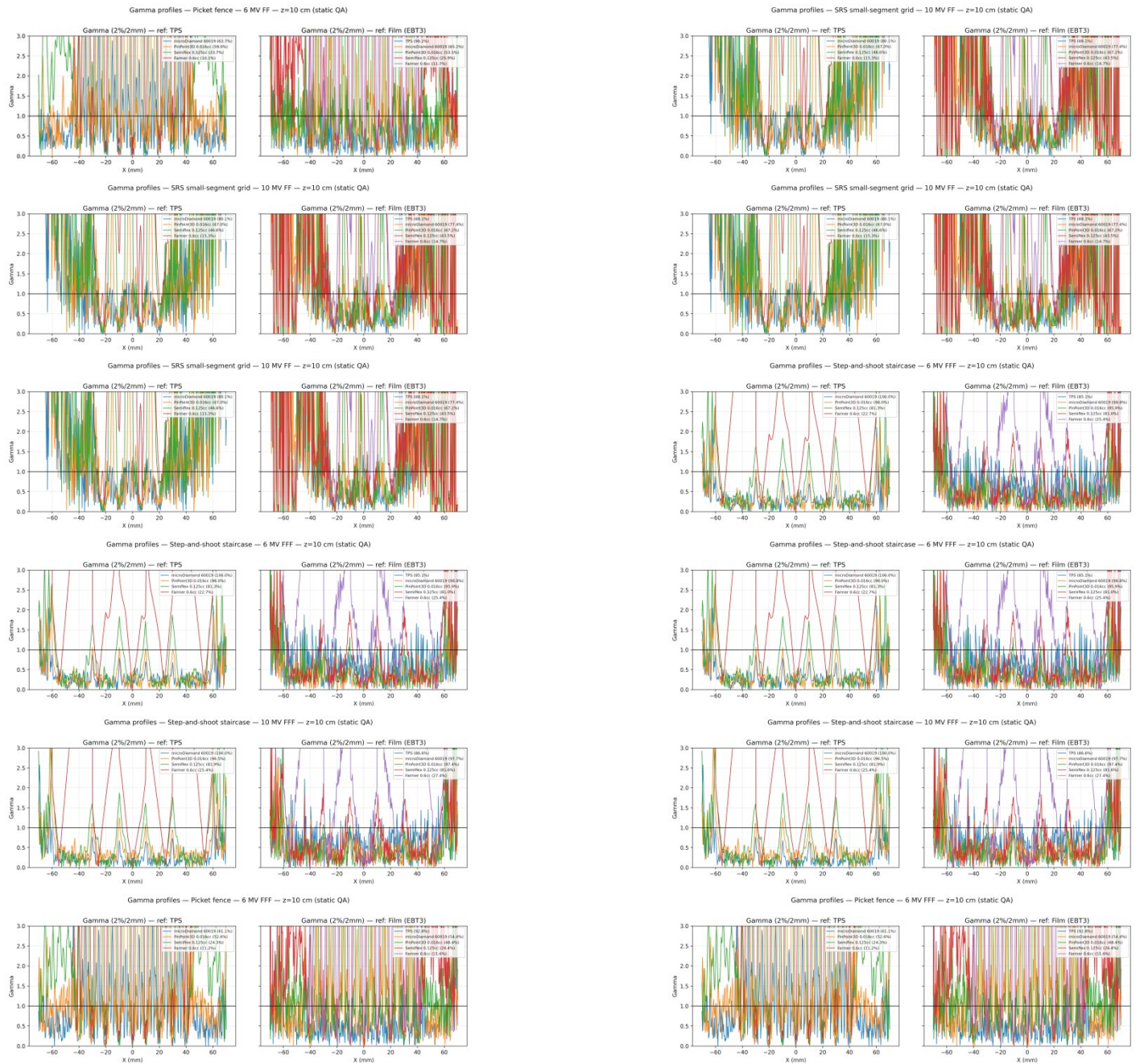


Figure 10: Local 1D gamma profiles for static QA patterns at $z = 10$ cm (TPS- and film-referenced). The figure summarizes in-plane gamma-index distributions computed along the central scan line for three representative static modulation patterns picket-fence, SRS small-segment grid, and step-and-shoot staircase for 6 MV and 10 MV photon beams (FF and FFF, as indicated in each panel). For each pattern and beam quality, gamma was evaluated using the local criterion (shown in the panel titles) against two references: TPS (left sub-panel) and Gafchromic EBT3 film (right sub-panel). The horizontal line at $\gamma = 1$ indicates the pass/fail threshold. Colored curves correspond to the evaluated dosimetry systems (microDiamond 60019, PinPoint 3D 0.016 cc, Semiflex 0.125 cc, Farmer 0.6 cc, and the corresponding reference), highlighting increased γ excursions in highly modulated/high-gradient regions most pronounced for the larger-volume chambers and improved agreement for high-resolution dosimeters (microDiamond and film).

PDD: good agreement at depth, with expected build-up divergences.

In our study, microDiamond 60019 was used as the PDD reference. Beyond dm_{max} , the agreement between ionization chambers and microDiamond was consistently good at clinical

depths, with differences typically within -0.1 – 0.9% at 10 – 20 cm (energy- and chamber-dependent). This behavior is expected because depth-dose gradients are relatively shallow at depth, so volume-averaging has a reduced impact, in line with the physical considerations highlighted in the small-field Code of Practice IAEA/AAPM TRS-483 [1].

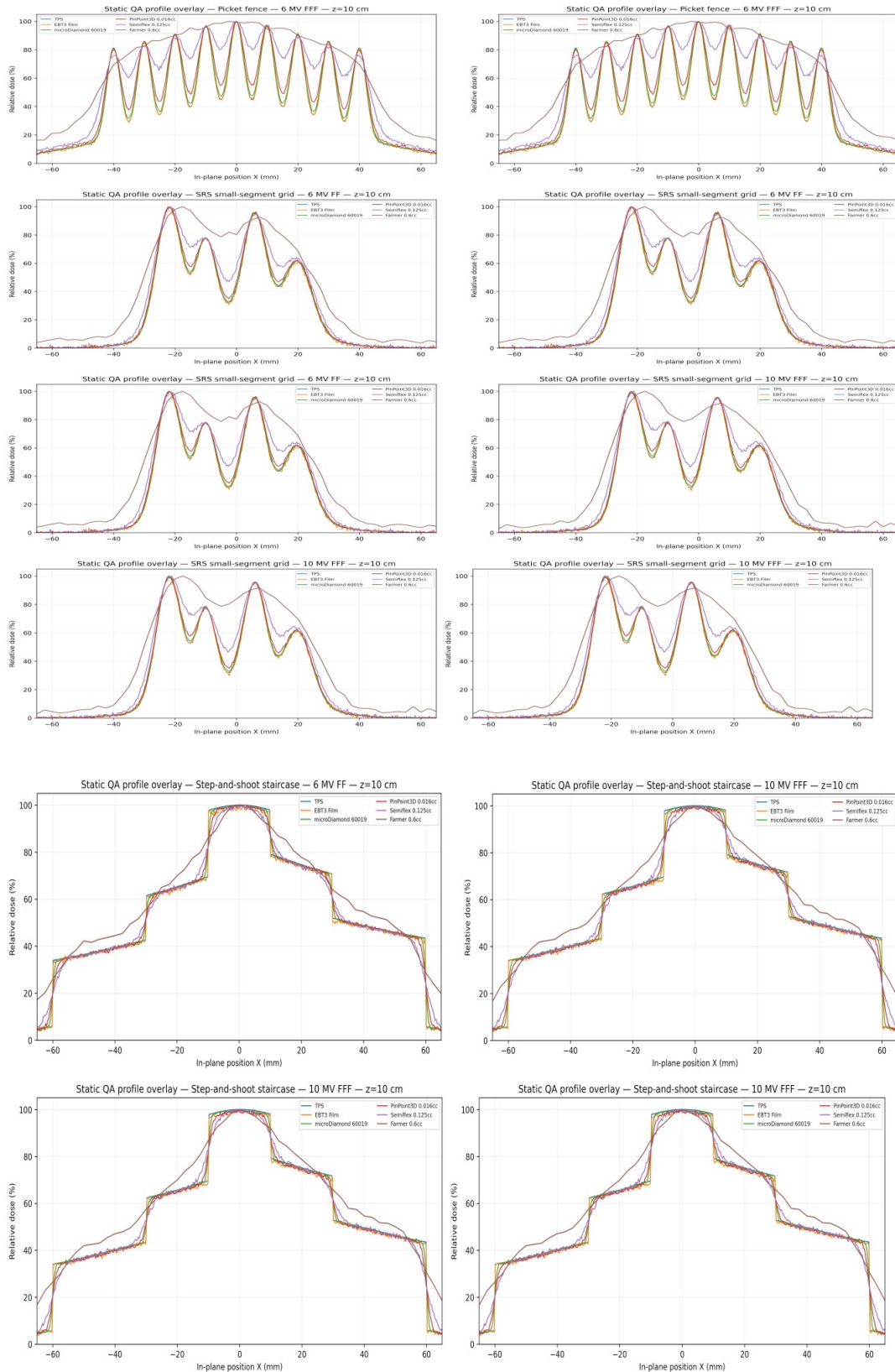


Figure 11: Static QA profile overlays (in-plane, $z = 10$ cm) illustrating detector-dependent spatial averaging in modulated static fields. Normalized 1D in-plane dose profiles are shown for three representative static test patterns: (a) picket-fence and (b) SRS small-segment grid (upper panel), and (c) step-and-shoot staircase (lower panel), each delivered with 6 MV and 10 MV photon beams (FF and FFF, as indicated in the subplot titles). Curves are overlaid for RayStation TPS, Gafchromic EBT3 film, microDiamond 60019, PinPoint 3D (0.016 cc), Semiflex (0.125 cc), and Farmer (0.6 cc), all normalized to the local maximum ($\sim 100\%$). High-resolution detectors (film and microDiamond) preserve sharper modulation peaks/valleys, whereas increasing ionization-chamber volume (PinPoint \rightarrow Semiflex \rightarrow Farmer) produces progressively stronger volume-averaging, visible as reduced peak-to-valley contrast, broadened transitions, and smoothing of fine structure most pronounced for the SRS-type pattern.

By contrast, larger divergences occurred in the build-up region ($\approx 0.5\text{--}1$ cm), where the dose gradient is steep and measurements become highly sensitive to (i) finite detector size (volume averaging), (ii) effective point of measurement / detector-dependent depth offset, and (iii) depth sampling resolution. TRS-483 explicitly emphasizes these limitations in high-gradient regions and the increasing influence of detector perturbation/averaging as fields become small [1,24]. Consistently, the Farmer chamber (0.6 cc) exhibited the largest build-up discrepancies, which is expected given its large sensitive volume and is aligned with small-field guidance that discourages using Farmer-type chambers in regions dominated by steep gradients and loss of lateral charged particle equilibrium [1]. These findings also match the broader small-field dosimetry framework introduced by Alfonso et al., where detector-dependent response and correction factors become increasingly important as conditions depart from reference-field assumptions effects that are most visible in steep-gradient regions and small apertures [2]. Finally, several experimental studies on the microDiamond and other small-field detectors have reported improved stability and robustness of high-resolution dosimeters compared with conventional ionization chambers in high-gradient regions (build-up and penumbra), while also confirming that even small-volume chambers remain more sensitive to positioning uncertainties and volume-averaging-induced smoothing than truly high-resolution detectors [11,25]. From a practical standpoint, PTW's small-field application guidance further emphasizes that finite detector volume can distort the apparent shape of a PDD, particularly around the depth of maximum dose and in steep-gradient regions, supporting a cautious interpretation of build-up discrepancies when using larger-volume chambers.

Lateral profiles: penumbra as the discriminative region, stable performance ranking

In our dataset, the largest inter-detector discrepancies for lateral profiles occur in the penumbra (high-gradient region), which is also where local 1D gamma failures concentrate for 3×3 and 5×5 cm² [Figures 7, 8]. This behavior is consistent with the small-field literature, where finite detector size and positioning sensitivity primarily manifest as penumbra broadening/smoothing, while the central plateau is comparatively less discriminative.

A directly comparable Elekta Versa HD study (6 MV and 6 MV FFF) by Monasor-Denia et al. reported that profile-width metrics diverge most for the smallest fields, and they explicitly observed that Semiflex 3D tends to overestimate the penumbra for 0.6×0.6 cm². Quantitatively, for 6 MV they reported R100 ≈ 0.49 cm (microDiamond), 0.42 cm (diode E), 0.47 cm (Semiflex 3D) and R50 ≈ 0.76 cm (microDiamond), 0.74 cm (diode E), 0.78 cm (Semiflex 3D), while for 6 MV FFF they reported R100 ≈ 0.48 cm (microDiamond), 0.41 cm (diode E), 0.47 cm (Semiflex 3D) and R50 ≈ 0.74 cm (microDiamond), 0.73 cm (diode E), 0.78 cm (Semiflex 3D). They further noted that microDiamond shows the largest relative dose difference at R100 for the 0.6×0.6 cm² field ($\approx 5.3\%$ at 6 MV and $\approx 4.5\%$ at 6 MV FFF), i.e., again highlighting the edge/penumbra as the most sensitive zone [26]. These findings match our qualitative ranking in [Figures 7, 8]: microDiamond and film remain the most “edge-faithful” references, whereas

Farmer exhibits the strongest penumbra broadening, and Semiflex sits intermediate, which is the expected hierarchy under dominant volume-averaging. The sensitivity of the penumbra to detector size and edge effects is also a well-established result in classic small-field detector comparisons; for instance, Wilcox & Daskalov showed that different detectors can yield measurably different penumbra widths, and reported diode-based penumbra values of about 2.6–2.9 mm for small ($\approx 2\times 2$ cm²) photon fields depending on diode type and beam energy again emphasizing that the gradient region is where detector-dependence is largest [27].

Finally, methodological work on profile measurements underlines why these discrepancies appear specifically at the edges: Wegener & Sauer explicitly target energy-response distortions in profile measurements (i.e., the penumbra/tails), proposing a correction approach based on combining detector types consistent with our observation that agreement improves with field size and is penumbra-driven [28].

Spatial Distribution of Gamma Failures in Small-Field Profiles

In gamma analysis of lateral beam profiles, failures are expected to cluster mainly in the penumbra (80–20% regions) and, to a lesser extent, in the off-axis tails, while the central high-dose plateau typically remains passing, because gamma is intrinsically more sensitive to small spatial mismatches in steep dose-gradient regions than in low-gradient plateaus [29]. This is the standard small-field behavior because the penumbra combines steep dose gradients, sub-millimetric positioning sensitivity, and (for ion chambers) finite-volume averaging, all of which directly worsen local gamma in edge regions [1,30].

Experimental evidence supports this interpretation. International small-field dosimetry guidance emphasizes that, as field size decreases, the largest profile discrepancies are expected at the field edges because measurements become increasingly governed by detector volume averaging/finite sensitive volume, detector perturbations, lateral charged-particle disequilibrium (LCPE), and partial source occlusion effects that are most visible in the penumbra rather than in the central plateau [1,31]. Consistently, the literature on lateral profile corrections explicitly notes that TRS-483 (and related standards) recommend correcting lateral profiles measured with small ionization chambers to remove detector-dependent volume-averaging and density effects, which otherwise bias the penumbra region [32].

Similarly, detector-comparison studies for small 6 MV and 6 MV FFF beams (including Versa-HD-type datasets) show that differences between detectors are detector-type dependent and become most relevant in small-field profile measurements, motivating the use of high-resolution detectors (e.g., diamond/diodes/film) when accurate edge/penumbra characterization is needed [26].

Output factors et FOC : cohérence TRS-483 et intérêt pratique du daisy-chain.

The measured small-field output factors (OFs) follow trends

fully consistent with the TRS-483 framework, which highlights the increasing impact of detector-related effects (finite sensitive volume/volume averaging and detector perturbations) as field size decreases [1–3]. To strengthen the normalization in the extreme small-field domain ($\leq 3 \times 3 \text{ cm}^2$), we applied a daisy-chain approach by linking the smallest fields to the reference field through an intermediate $5 \times 5 \text{ cm}^2$ field, which helps avoid using a single detector outside its optimal operating range and improves the robustness of inter-detector comparisons [1,5]. Using EBT3 film as the reference, detector dependence is maximal at $1 \times 1 \text{ cm}^2$ and rapidly decreases with field size: the microDiamond shows a small but systematic over-response of +1.6% (e.g., 6 MV FF: 0.735 vs 0.723 for film; 10 MV FF: 0.714 vs 0.702), whereas the PinPoint 3D exhibits an under-response of -1.8% at 6 MV and up to -3.8% at 10 MV (e.g., 10 MV FF: 0.676 vs 0.702 for film) [10–12]. At $2 \times 2 \text{ cm}^2$, agreement improves markedly (microDiamond +0.2–0.3%, PinPoint -0.2 to -0.4%), while Semiflex retains the largest residual under-response (≈ -0.7 to -0.8%); by $3 \times 3 \text{ cm}^2$, all detectors converge toward film (typically $\leq 0.1\%$), and differences become practically negligible for $\geq 5 \times 5 \text{ cm}^2$ [3,10–12]. Overall, this hierarchy (microDiamond slightly >1 , ion chambers slightly <1 at the smallest fields, with a stronger effect at 10 MV) matches expected small-field behavior and supports the practical use of a combined high-resolution detector strategy together with daisy-chain normalization to improve the reliability of OFs and the associated output correction factors (OFCs) [1–3,5,10–12].

Motifs QA statiques : volume averaging et “modulation fidelity”

The three static MLC QA patterns used here (2-mm picket-fence slits, step-and-shoot staircase, and a $5 \times 5\text{-mm}^2$ SRS small-segment grid) were designed to stress steep gradients and rapidly varying fluence, so the dominant limitation is modulation fidelity (peak-valley contrast and edge sharpness) rather than absolute scaling. In our 1D local gamma evaluation at 10 cm depth (high-dose/high-gradient ROI), this translated into a clear detector hierarchy versus TPS: microDiamond achieved 97.0% (90.9–100) at 2%/2 mm and 98.9% (90.9–100) at 3%/3 mm, while PinPoint 3D reached 93.4% (77.3–100) and 98.4% (95.5–100), respectively; Semiflex and Farmer were substantially lower at 2%/2 mm (62.8% and 44.7% means) and improved but remained limited at 3%/3 mm (80.7% and 58.3%). This behavior is consistent with the expected impact of finite sensitive volume: increasing chamber volume (PinPoint \rightarrow Semiflex \rightarrow Farmer) smooths sharp modulation peaks/valleys and broadens transitions, which increases local γ excursions in the most modulated regions.

When film was used as the reference (higher spatial fidelity in steep gradients), gamma pass rates decreased across detectors (2%/2 mm means: microDiamond 76.0%, PinPoint 76.9%, Semiflex 58.3%, Farmer 43.4%), and even TPS vs film was limited (77.7% at 2%/2 mm; 87.9% at 3%/3 mm). This supports the interpretation that part of the apparent detector-to-TPS disagreement reflects TPS smoothing/modeling relative to high-resolution film response in high-gradient structures [33,34]. A closely related conclusion is reported in de Freitas Nascimento et al, where a high-resolution film-based QA approach showed edge/gradient sensitivity: their

profile-shape metrics (FWHM and penumbra-width indicators) were generally within $\sim 5\%$ versus a diode reference, with FWHM differences reported below $\sim 1.5\%$ for most cases, and they highlight that the most pronounced discrepancies appear in out-of-field/edge regions (e.g., OF 3% differences spanning large negative values for large fields and up to $\sim +20\%$ for the smallest $6 \times 6 \text{ mm}^2$ field) [35].

Clinical implications and recommendations

Detector choice for small-field commissioning and SRS QA. In fields at or below $\sim 3 \times 3 \text{ cm}^2$, your commissioning and QA conclusions can be dominated by detector physics rather than true beam/model differences. International guidance emphasizes that loss of lateral charged-particle equilibrium, partial source occlusion, and detector perturbation/finite-volume averaging become increasingly important as field size shrinks, so high-resolution detectors (diamond/diodes/film) are preferred for profiles and output factors in the smallest fields [1,31]. Practically, this means: use a high-resolution detector for small-field profiles (penumbra/shoulders) and OFs, and reserve conventional chambers for $\geq 3 \times 3 - 5 \times 5 \text{ cm}^2$ where volume averaging is less influential [1,31]. Use a TRS-483/Alfonso-consistent OFC workflow (and document it). For small-field output factors, TRS-483 operationalizes the Alfonso formalism through the use of machine-specific reference fields and output correction factors $k_{Q_{\text{clin}}, Q_{\text{ref}}}^{f_{\text{lin}}, f_{\text{ref}}}$ to correct detector response in clinical small fields [1,2,31,33]. Clinically, the safest practice is: (i) measure small-field OFs with an appropriate detector, (ii) apply the relevant TRS-483 correction factors (or an equivalent validated method), and (iii) keep a clear traceability chain in your commissioning report (detector type, field definitions, reference field, corrections used) [1,2,31,33]. Adopt a “daisy-chain” normalization when one detector cannot cover the whole field-size range reliably. A daisy-chain (small field \rightarrow intermediate field $\rightarrow 10 \times 10$) is a pragmatic way to reduce systematic bias when the detector suited to very small fields is not optimal for larger reference fields (or vice versa). This approach aligns with TRS-483’s emphasis on using detectors within their validated domain and maintaining consistent normalization across measurements [1,5,36]. Interpret gamma pass rates as a resolution/gradient test not a single pass/fail truth. Gamma metrics are inherently more sensitive in steep gradients (e.g., penumbra, high-modulation patterns), and “good” pass rates can mask clinically relevant errors if the evaluation setup is poorly chosen [37]. For patient-specific IMRT/VMAT QA, TG-218 recommends standardized methodology (dose thresholding, criteria selection, action/tolerance limits) and warns against practices that can hide delivery errors [33]. Clinically: keep the same gamma conventions across time (criteria, dose threshold, ROI), and complement pass rates with where failures occur (edges/valleys vs plateau) [33,37].

Cross-validate your small-field OF dataset against external benchmarks. Multicentre datasets show that systematic errors in OF measurement are common and that validated reference datasets can help detect outliers when commissioning SRT/SRS programs [22]. Using published multi-institution OF datasets (when matched by energy, MLC/collimation style, and

measurement geometry) as a sanity check is a low-effort, high-value clinical safeguard [22,38]. Use film strategically for “ground truth” spatial fidelity (with a rigorous protocol). Radiochromic film (e.g., EBT3) remains a strong option for high-gradient/static pattern verification because of its spatial resolution, but its accuracy depends on careful calibration and control of scanning/analysis uncertainties [39]. Clinically: use film to adjudicate edge/penumbra behavior or highly modulated test patterns, but avoid treating film as perfect quantify its uncertainty and keep protocol consistency (scanner warm-up, orientation, multi-channel/one-scan approach where applicable) [39].

CONCLUSION

This work provides a combined small-field dosimetry and static-pattern QA evaluation using EBT3 film, microDiamond, PinPoint 3D, and conventional ionization chambers across 6 and 10 MV photon beams. For output factors, detector dependence was largest at $1 \times 1 \text{ cm}^2$ and decreased rapidly with field size: relative to film, microDiamond showed a small, systematic over-response ($\sim +1.6\%$), while PinPoint 3D under-responded (up to $\sim -3.8\%$ at 10 MV), whereas agreement became clinically negligible from $\sim 3 \times 3 \text{ cm}^2$ and above. These findings are consistent with TRS-483 small-field behavior and support the practical value of a daisy-chain normalization to improve traceability when a single detector cannot reliably cover the full field-size range. In static MLC QA patterns, high-resolution detectors (microDiamond/film) better preserved

modulation fidelity, while larger chambers exhibited increasing smoothing and reduced gamma agreement in highly modulated regions, consistent with volume-averaging effects. Overall, the results reinforce that reliable commissioning and QA in SRS-relevant small fields require detector selection matched to spatial gradients, explicit reporting of field definitions and normalization strategy, and where appropriate TRS-483-consistent correction workflows to ensure robust, clinically transferable beam data.

DECLARATION OF COMPETING INTERESTS

The authors declare no competing interests.

ETHICAL STATEMENT

Not applicable.

COMPETING INTERESTS

The authors declare no conflict of interest.

FUNDING

None.

ACKNOWLEDGMENTS

None.

REFERENCES

1. IAEA. Dosimetry of Small Static Fields Used in External Beam Radiotherapy: An International Code of Practice for Reference and Relative Dose Determination (TRS-483). Vienna: International Atomic Energy Agency; 2017.
2. Alfonso R, Andreo P, Capote R, Huq MS, Kilby W, et al. A new formalism for reference dosimetry of small and nonstandard fields. *Med Phys.* 2008; 35:5179–5186.
3. Das IJ, Ding GX, Ahnesjö A. Small fields: nonequilibrium radiation dosimetry. *Med Phys.* 2008; 35:206–215.
4. Bannan A, Sekkat H, El Mouden O, Khallouqi A, Baydaoui RE, et al. Investigating the performance of the novel microSilicon diode detector for high-resolution dosimetry in radiotherapy: Flat and FFF beams across multiple energies. *Nucl Instrum Methods Phys Res B.* 2026; 570:165945.
5. Sekkat H, Khallouqi A, El Mouden O, Bannan A, Berrada Y, et al. Novel correction model for microDiamond detector response in small-field radiotherapy: demonstrated improvements over the Daisy Chain method. *J Radioanal Nucl Chem.* 2026.
6. Alashkar EM, Abdelhafez HM, Kenawy MA, Hassan GM, Ereiba KT, et al. Comparison flattening filter and flattening filter-free techniques in small-fields dosimetry with various types of detectors. *Asian Pac J Cancer Prev.* 2024; 25:2105–2112.
7. Francescon P, Kilby W, Satariano N, Cora S. Monte Carlo simulated correction factors for machine specific reference field dose calibration and output factor measurement using fixed and iris collimators on the CyberKnife system. *Phys Med Biol.* 2012; 57:3741–3758.
8. Martin-Martin G, Walter S, Guibelalde E. Dosimetric impact of failing to apply correction factors to ion recombination in percentage depth dose measurements and the volume-averaging effect in flattening filter-free beams. *Phys Med.* 2020; 77:176–180.
9. Ringholz J, Sauer OA, Wegener S. Small field output correction factors at 18 MV. *Med Phys.* 2023; 50:7177–7191.
10. Pappas E, Maris TG, Zacharopoulou F, Papadakis A, Manolopoulos S, et al. Small SRS photon field profile dosimetry performed using various detectors: Analysis and intercomparison. *Med Phys.* 2008; 35:4640–4648.
11. Reggiori G, Stravato A, Pimpinella M, Lobefalo F, Coste VD, et al. Use of PTW-microDiamond for relative dosimetry of unflattened photon beams. *Phys Med.* 2017; 38:45–53.
12. Hartmann GH, Zink K. A Monte Carlo study on the PTW 60019 microDiamond detector. *Med Phys.* 2019; 46:5159–5172.
13. Devic S. Radiochromic film dosimetry: Past, present, and future. *Phys Med.* 2011; 27:122–134.
14. Niroomand-Rad A, Chiu-Tsao ST, Grams MP, Lewis DF, Soares CG, et al. Radiochromic film dosimetry: An update to TG-55. *Med Phys.* 2020; 47:5986–6025.
15. Niroomand-Rad A, Blackwell CR, Coursey BM, Gall KP, Galvin JM, et al. Radiochromic film dosimetry: Recommendations of AAPM TG-55. *Med Phys.* 1998; 25:2093–2115.
16. Lewis D, Micke A, Yu X, Chan MF. An efficient protocol for radiochromic film dosimetry combining calibration and measurement in a single scan. *Med Phys.* 2012; 39:6339–6350.
17. Chang L, Chen PY, Yeh SA, Kang CL, Su CT, et al. Adaptive calibration of Gafchromic EBT3 film using generalized additive neural networks. *Sci Rep.* 2025; 15:8208.
18. Bannan A, Sekkat H, El Mouden O, Khallouqi A, Baydaoui RE, et al. Assessment of response accuracy of the novel microSilicon diode detector for small field dosimetry applications in radiotherapy. *Silicon.* 2025; 17:4111–4120.
19. Fontana TS, Bueno KP, Albino LD, Roesler EH, Santos MF, et al. Comparison between radiochromic film and diode detector during commissioning of small field radiosurgery cones. *Braz J Radiat Sci.* 2022; 10.
20. Chang L, Yeh SA, Ho SY, Ding HJ, Chen PY, et al. An adaptive method for recalibrating Gafchromic EBT3 film. *Nucl Instrum Methods Phys Res A.* 2021; 1007:165435.
21. Kannan M, Saminathan S, Chandraraj V, Ganesh KM. Determination of small-field output factors for beam-matched linear accelerators using various detectors. *Rep Pract Oncol Radiother.* 2023; 28:241–254.
22. Dufreneix S, Bellec J, Josset S, Vieilleuvre L. Field output factors for small fields: A multicentre study. *Phys Med.* 2021; 81:191–196.
23. Hussain S, Longo M, Cora S, Francescon P. Small-field output factor determination for Versa HD beams with various detectors.
24. Palmans H, Andreo P, Huq MS, Seuntjens J, Christaki KE, et al. Dosimetry of small static fields: Summary of TRS-483. *Med Phys.* 2018; 45:e1123–e1145.
25. Fenwick JD, Kumar S, Scott AJD, Nahum AE. Using cavity theory to describe detector response in non-equilibrium small fields. *Phys Med Biol.* 2013; 58:2901–2923.
26. Denia PM, García MCC, García CM, Higuera JDQ, Blancas NM, et al. Comparison of detector performance in small photon beams. *PLoS One.* 2019; 14:e0213253.
27. Wilcox EE, Daskalov GM. Evaluation of GAFCHROMIC EBT film for CyberKnife dosimetry. *Med Phys.* 2007; 34:1967–1974.
28. Wegener S, Sauer OA. Energy response corrections for profile measurements using different detectors. *Med Phys.* 2018; 45:898–907.
29. Low DA, Harms WB, Mutic S, Purdy JA. A technique for quantitative evaluation of dose distributions. *Med Phys.* 1998; 25:656–661.
30. Wuerfel JU. Dose measurements in small fields. 2013.
31. Das IJ, Francescon P, Moran JM, Ahnesjö A, Aspradakis MM, et al. AAPM TG-155: Megavoltage photon beam dosimetry in small fields. *Med Phys.* 2021; 48:e886–e921.
32. Schönfeld AB, Mund K, Yan G, Looe HK, Poppe B. Corrections of photon beam profiles using neural networks. *J Appl Clin Med Phys.* 2021; 22:64–71.
33. Deng J, Liu S, Huang Y, Li X, Wu X. Evaluating TG-218 recommendations using SunCHECK. *J Appl Clin Med Phys.* 2024; 25:e14277.
34. Ezzell G, Burmeister J, Dogan N, LoSasso T, Mechalakos J, et al. IMRT commissioning: AAPM TG-119. *Med Phys.* 2009; 36:5359–5373.
35. de Freitas Nascimento L, Castellano F, Goossens J, van Dijk A, Leblans P, et al. Investigation of radiophotoluminescence films in radiotherapy. *Nucl Instrum Methods Phys Res A.* 2022; 1028:166349.
36. Lárraga-Gutiérrez JM. Experimental determination of field factors for small radiotherapy beams using daisy chain method. *Phys Med Biol.* 2015; 60:5813.
37. Low DA, Harms WB, Mutic S, Purdy JA. A technique for quantitative evaluation of dose distributions. *Med Phys.* 1998; 25:656–661.
38. Russo S, Reggiori G, Cagni E, Clemente S, Esposito M, et al. Small field output factors evaluation with a microDiamond detector. *Phys Med.* 2016; 32:1644–1650.
39. Dreindl R, Georg D, Stock M. Radiochromic film dosimetry: Precision and accuracy considerations. *Z Med Phys.* 2014; 24:153–163.